Materials Science & Engineering A 676 (2016) 450–462

Contents lists available at ScienceDirect

Materials Science & Engineering A

journal homepage: www.elsevier.com/locate/msea

Fast-condensing nanofoams: Suppressing localization of intense stress waves

Cang Zhao [a], Yu Qiao [a,b,*]

[a] Department of Structural Engineering, University of California – San Diego, La Jolla, CA 92093-0085, USA
[b] Program of Materials Science and Engineering, University of California – San Diego, La Jolla, CA 92093, USA

ARTICLE INFO

Article history:
Received 5 July 2016
Received in revised form
1 September 2016
Accepted 2 September 2016
Available online 4 September 2016

Keywords:
Nanofoam
Size effect
Energy absorption
Localization
Stress wave

ABSTRACT

We investigated the propagation of intense stress waves across silica nanofoams, with the pore size ranging from ~50 nm to ~1 μm and the porosity of ~60%. The experimental results showed that if the pore size was relatively large, the stress wave remained localized and its energy was dissipated in narrow bands; if the pore size was below ~200 nm, however, the stress wave was homogenized in a broad area and consequently, bulk distributed energy absorption was promoted and the maximum transmitted-wave pressure was significantly reduced. We attribute this phenomenon to the fast condensation of the smallest pores at the wave front. The ability of nanofoams to promote widespread energy absorption may enable efficient stress-wave mitigation techniques. The classic Grady model was modified to take account for the nanopore size effect.

1. Introduction

Associated with intense dynamic shear loading, a stress wave can be localized [1,2]; that is, the wave front may become non-uniform in transverse directions. An intense stress wave is often nonlinear; i.e., nonlinear material behaviors, e.g. internal damaging, dominate the wave propagation and dissipation. Under this condition, many concepts of linear wave theory, such as acoustic impedance and wave energy conservation, may break down. For instance, as a nonlinear stress wave advances into a solid material, it can cause plastic yielding, micro-cracking, and/or local phase transformation [3–7]; in a foam material, it may trigger cell buckling and ligament rupture [8,9]; in a granular material, it can activate rearrangement of close-packed components [10,11]. The nonlinearity is often coupled with the stress wave localization [12–14]; i.e., an initially uniform wave front may become localized and the wave energy is dissipated in a number of narrow zones, e.g. shear bands [3,10,15,16]. The instability of stress wave can be caused by either material instability or geometrical instability [1]. Over the years, the stability of stress waves was extensively investigated [1,10,11,17–21]. Shear-band nucleation, propagation, and morphology change were related to materials properties and loading modes. However, there still lack efficient methods to "disperse" intense stress waves and to promote widespread energy absorption.

For each material and loading condition, when an intense stress wave is localized, the shear deformation zone (SDZ) has a characteristic width, w, ranging from a few nm in metallic glass [22] to hundreds of μm in foam materials [8] or granular materials [23,24]. For brittle solids, based on the equilibrium condition of kinetic energy and strain energy, Grady [25,26] developed a model to predict the fragment length:

$$L = \left(\frac{\sqrt{24} K_c}{\rho C \dot{\varepsilon}} \right)^{2/3} \quad (1)$$

where K_c is the fracture toughness, ρ is the mass density, C is the speed of sound, and $\dot{\varepsilon}$ is the strain rate. This framework can be applied to analyze both the spacing and the size of SDZ. It captures the effects of strain rate and resistance to shear [27,28]. The Grady model has successfully explained many experimental observations of solid and porous materials [27,29–31]. It suggests that the SDZ size (w) is independent of the characteristic length of the material, e.g. the pore size (d).

Foams are solid materials containing empty cells or pores [32]. A few examples of foams include bones [33,34], woods [34,35], carbon nanotube bundles [36], and porous polymers/metals/ceramics [37–39]. In general, foams are lightweight. They are widely applied for thermal insulation, acoustic damping, and impact and vibration protection [32,40]. In a foam material, if a stress wave becomes localized, catastrophic failure would take place in narrow shear bands, with the majority of the protection capacity being "wasted". In a regular foam material where the pore size is

* Corresponding author at: Department of Structural Engineering, University of California – San Diego, La Jolla, CA 92093-0085, USA.
E-mail address: yqiao@ucsd.edu (Y. Qiao).

http://dx.doi.org/10.1016/j.msea.2016.09.021
0921-5093/

Nomenclature

A	cross-sectional area used in the calculation of acoustic impedance
A_b	cross-sectional area of the Hopkinson bars
C	speed of sound used in the Grady model
C_b	speed of sound of the Hopkinson bars
d	pore size
D	diameter of the loading rod
D_r	inner diameter of the support ring
E_b	Young's modulus of the Hopkinson bars
F	peak force
K_c	fracture toughness
L	fragment length
m	sample mass
p	porosity
p_2	nominal two-dimensional porosity of a nanofoam sample
p_2^*	nominal two-dimensional porosity of a pristine nanofoam sample
P_{Hg}	infiltration pressure of mercury
P_{Pi}	Average maximum incident-wave pressure
P_{t0}	equivalent maximum normal stress
P_{tc}	maximum transmitted-wave pressure in dynamic compression
P_{ts}	maximum transmitted-wave pressure in dynamic shearing
P_w	stress-wave pressure
r	radius of the loading rod
S_0	quasi-static shear strength
t	sample thickness
T	temperature
T_P	pulse duration
U	energy associated with stress wave
U_i	energy associated with incident stress wave
U_k	kinetic energy associated with local particle velocity
U_r	energy associated with reflected stress wave
U_s	strain energy associated with local deformation
U_t	energy associated with transmitted stress wave
v	impact velocity of the striker
V	volume of the material that undergoes permanent structural changes
w	shear-deformation-zone size
z	acoustic impedance of nanofoam sample
β	energy dissipation factor
ε	strain
$\dot{\varepsilon}$	strain rate
ρ	mass density (mass divided by sample volume)
ρ_b	mass density of the Hopkinson bars
ρ_s	mass density of solid amorphous silica
ς	pressure reduction factor

relatively large, e.g. comparable with or larger than the typical SDZ size, the cell buckling at the stress wave front may be viewed as a process that reduces the shear resistance; thus, wave energy dissipation tends to be limited within a number of narrow bands. In the current study, we investigate nanofoams in which the pores are nano-sized, much smaller than the typical SDZ size. In such a material, cell buckling may be viewed as a fast condensation mechanism, which increases the effective local shear resistance. As the shear banding is suppressed, bulk-distributed energy absorption may be promoted.

2. Methodology

2.1. Materials and specimens

In the current investigation, we processed a set of monolithic silica foam samples. The pore formation was achieved by sol-gel methods [39,41,42], and the porous structure was precisely controlled by a subcritical calcination (SCC) process [43]. The details of the sample preparation have been documented in Appendix A.

The pore formation agents were polyethylene glycol (PEG) for large pores, or potassium silicate for small nanopores. After phase separation, they were eliminated through acid washing. Then, the samples were dried at 80 °C for 3 days in a VWR 1330GM oven, and subcritically calcinated at temperatures slightly higher than the glass transition point of amorphous silica glass, 1200 °C, for 1 h in a MTI GSL-1700X horizontal tube furnace. The ramp rate was initially set as 3 °C/min; and when the temperature was 100 °C away from the target temperature, the ramp rate was reduced to 1 °C/min. After the SCC procedure, cooling was conducted at a rate of 3 °C/min to minimize the residual stress.

The processing conditions and the key material parameters of the silica nanofoams are shown in Table 1. The testing samples were disk-shaped, with the diameter of ~23 mm and the thickness of 4.50 mm. Fig. 1a shows the X-ray diffraction (XRD) analysis results. Fig. 1(b–d) show the morphology of silica nanofoams.

2.2. Mechanical testing

2.2.1. Shear-promotion-support-ring system

The shear-promotion-support-ring (SPSR) system, as shown in Fig. 2a, included a front part and a rear part made of 17–4 PH stainless steel. As depicted in Fig. 2b, a silica nanofoam disk was mounted between the front part and the rear part, with an thin layer of petrolatum applied on each interface to reduce potential friction and to smoothen stress wave transmission. A loading rod with the outer diameter of 12.7 mm was compressed against the surface of the sample. At the back of the silica disk, the support ring and the steel plate on the rear part were used to support the sample. The inner diameter of the support ring was 13.1 mm, slightly larger than the outer diameter of the loading rod; the

Table 1
Processing conditions and properties of silica nanofoams.

Component mass ratio	TMOS to PEG	Colloidal silica to potassium silicate							
	5.5:1.0	1.3:98.7	7.5:92.5	12.5:87.5	17.0:83.0	22.5:77.5	27.5:72.5	35:65	40:60
SCC temperature (°C)	1230	1260	1262	1260	1258	1254	1251	1239	1228
Pore size range	[780,1980]	[240,390]	[190,290]	[150,220]	[130,180]	[100,140]	[70,100]	[60,80]	[40,60]
Average pore size (nm)	1380 ± 600	315 ± 75	240 ± 50	185 ± 35	155 ± 25	120 ± 20	85 ± 15	70 ± 10	50 ± 10
Porosity (%)	59.6 ± 2.7	62.7 ± 0.9	61.6 ± 0.9	60.7 ± 1.2	59.5 ± 0.8	62.4 ± 1.4	59.1 ± 2.0	60.0 ± 1.5	60.0 ± 1.3

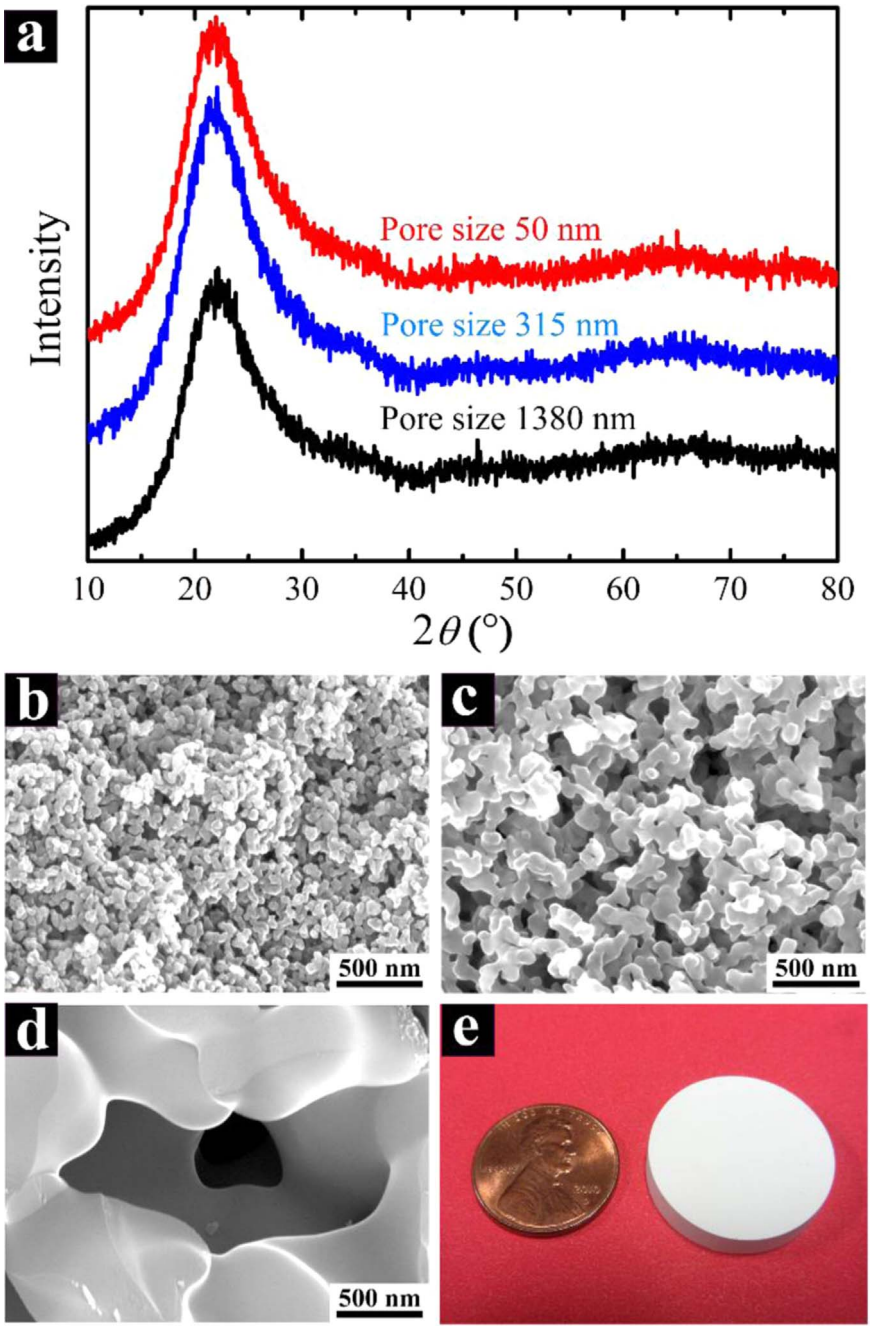

Fig. 1. Silica nanofoams. (a) Typical x-ray diffraction curves. SEM images of silica nanofoam samples with the average pore sizes of (b) 50 nm, (c) 155 nm, and (d) 1.4 μm, respectively. (e) Photo of a monolithic silica nanofoam disk.

outer diameter was 25.0 mm; the thickness was 3.0 mm. The diameter of the steel support plate was 43.0 mm; the thickness was 3.0 mm. The centers of the loading rod and the support ring were accurately aligned by the guiding parts, with the gap width between the outer surface of the loading rod and the inner surface of the support ring being 0.20 mm along all the directions. The parts were designed to reduce the potential bending of the nanofoam sample during testing. The lateral surface of nanofoam sample was loosely confined by a soft polyurethane ring, with the initial inner diameter of 19.1 mm and outer diameter of 22.2 mm. The design of SPSR was inspired by the hat-shaped specimens [1,10,44]: shear deformation could be promoted in the narrow circular band in-between the outer surface of loading rod and the inner surface of SPSR.

2.2.2. Quasi-static shear test

As a reference test, the silica nanofoams were sheared by quasi-static loadings. As shown in the inset of Fig. 3, a silica nanofoam disk was sandwiched in-between a stainless steel loading rod and a stainless steel SPSR. The inner diameter of the SPSR was 13.1 mm, slightly larger than the outer diameter of the loading rod, $2r = 12.7$ mm. The loading rod and the SPSR were concentric. The gap width, i.e. the difference between the radius of the loading rod and the inner radius of the SPSR, was 0.20 mm. In a Type-5582 Instron machine, the loading rod compressed the silica sample, with the loading/unloading rate of 0.01 mm/min. Shear instability was triggered in the narrow circular band between the outer surface of loading rod and the inner surface of SPSR. Fig. 3 shows typical load-displacement curves. The effective quasi-static shear strength is defined as

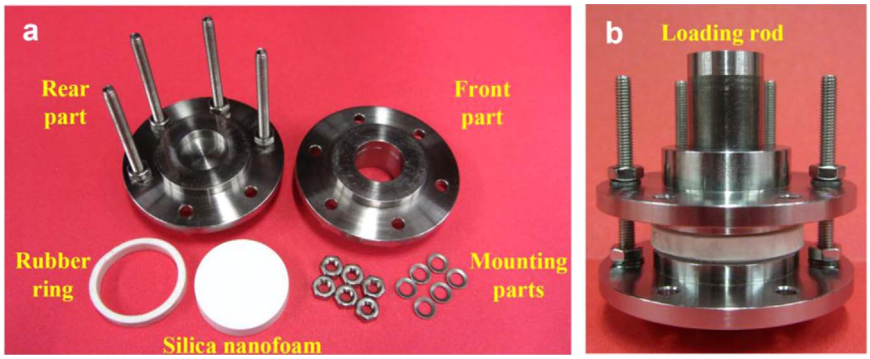

Fig. 2. Photos of the shear-promotion-support-ring (SPSR) system. (a) The system components and a silica nanofoam sample; the diameter of the silica nanofoam sample is ~23 mm. (b) A silica nanofoam sample mounted in the SPSR system, with the steel loading rod compressing the sample. The diameter of the rod is 12.7 mm and the inner diameter of the support ring on the rear part is 13.1 mm.

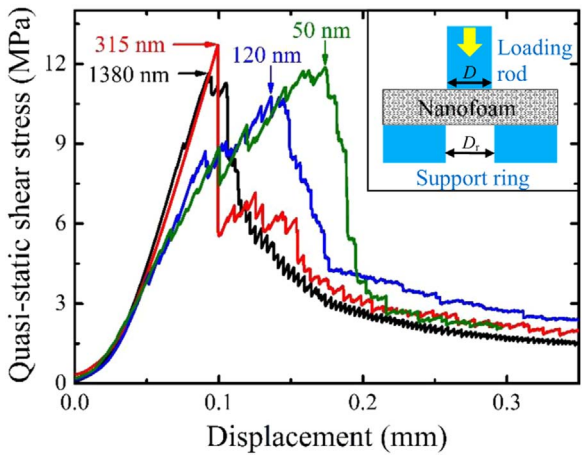

Fig. 3. Typical load-displacement curves under quasi-static shear condition. The arrows indicate the average pore sizes of the samples. The inset shows the schematic of the testing setup; the outer diameter of the compression rod is D=12.7 mm; the inner diameter of the support ring is D_r=13.1 mm; the loading/unloading rate is 0.01 mm/min.

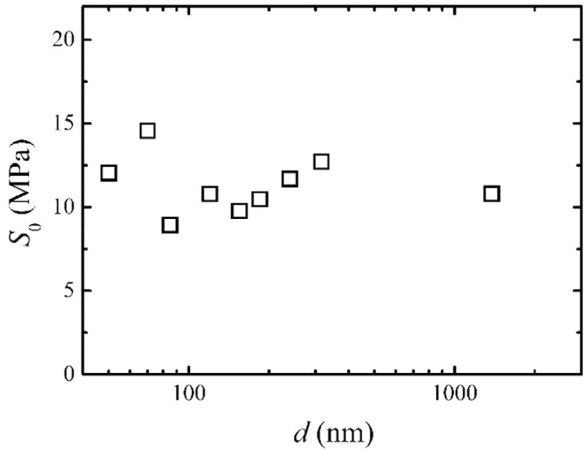

Fig. 4. Quasi-static shear strength, S_0, as a function of the average pore size, d.

$$S_0 = \frac{F}{2\pi rt} \tag{2}$$

where F is the measured peak loading at the onset of shear failure and t is the sample thickness. Table 2 and Fig. 4 show the quasi-static shear strength (S_0).

2.2.3. Dynamic compression test

As another reference test, we also investigated the behaviors of silica nanofoams under one-dimensional compressive stress waves, by using a Split Hopkinson Bar (SHB) system [45–47]. The details of the SHB system were documented in Appendix B. A 62.8 g titanium (Ti) tube striker was projected by a gas chamber and impacted the stainless steel incident bar. Upon impact, a high-pressure stress wave was generated and propagated along the incident bar [47]. In all the tests, the striker speed was kept at ~8.5 m/s. On the other end of the incident bar, a silica nanofoam disk sample was firmly attached, supported by a stainless steel transmitted bar from the back. The stress wave entered into the silica sample, and eventually transmitted to the transmitted bar. The diameters of all the bars were 12.7 mm; the lengths of the incident and the transmitted bars were 178 cm and 152 cm, respectively. The incident, reflected and transmitted-wave profiles were measured by the strain gauges mounted on the incident bar and the transmitted bar, respectively, as shown in Fig. 5. The transmitted-wave pressures (P_{tc}, the peak pressure in the wave profile) were summarized in Table 2 and Fig. 6.

2.2.4. Dynamic shear test

Dynamic shear tests were conducted on silica nanofoam disks by using the same SHB system as in Section 2.2.3, except that the sample was supported by a stainless steel SPSR from the back. The SPSR was the same as the support ring in Section 2.2.2. The striker speed was maintained at ~8.5 m/s. The gap width between the outer surface of incident bar and the inner surface of SPSR was set as 0.20 mm. Fig. 7 shows the incident, reflected and transmitted-wave profiles, respectively. The transmitted-wave pressures (P_{ts},

Table 2
Testing results of silica nanofoams.

d (nm)	1380 ± 600	315 ± 75	240 ± 50	185 ± 35	155 ± 25	120 ± 20	85 ± 15	70 ± 10	50 ± 10
p (%)	59.6 ± 2.7	62.7 ± 0.9	61.6 ± 0.9	60.7 ± 1.2	59.5 ± 0.8	62.4 ± 1.4	59.1 ± 2.0	60.0 ± 1.5	60.0 ± 1.3
p_i (MPa)	32.7 ± 0.6	32.3 ± 0.6	31.4 ± 1.2	31.1 ± 0.4	31.3 ± 0.6	32.7 ± 0.6	29.1 ± 0.3	31.3 ± 0.5	31.6 ± 0.2
S_0 (MPa)	10.8	12.7	11.7	10.5	9.8	10.8	9.0	14.6	12.0
P_{tc} (MPa)	29.9	30.0	30.1	29.6	30.6	28.6	29.4	28.3	28.5
P_{ts} (MPa)	29.3 ± 4.1	17.8 ± 1.9	16.4 ± 1.5	11.9 ± 0.9	13.4 ± 0.1	10.5 ± 0.8	11.2 ± 1.0	11.0 ± 1.4	13.8 ± 1.0
β	0.35 ± 0.14	0.75 ± 0.04	0.82 ± 0.02	0.87 ± 0.02	0.85 ± 0.01	0.90 ± 0.01	0.89 ± 0.02	0.89 ± 0.01	0.82 ± 0.01

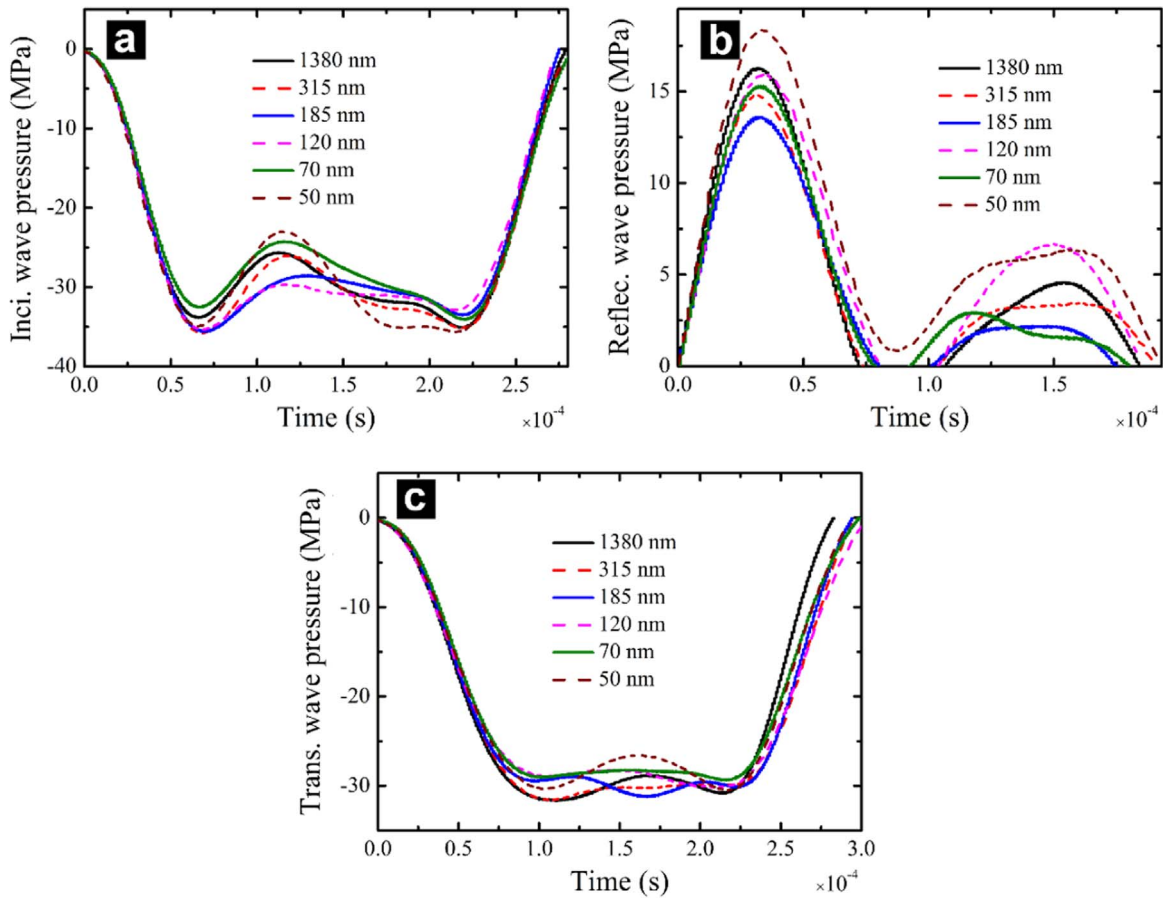

Fig. 5. Typical profiles of (a) incident, (b) reflected, and (c) transmitted stress waves under dynamic compression conditions. The legends indicate the average pore sizes of silica foams. The impact rate of striker is ~8.5 m/s.

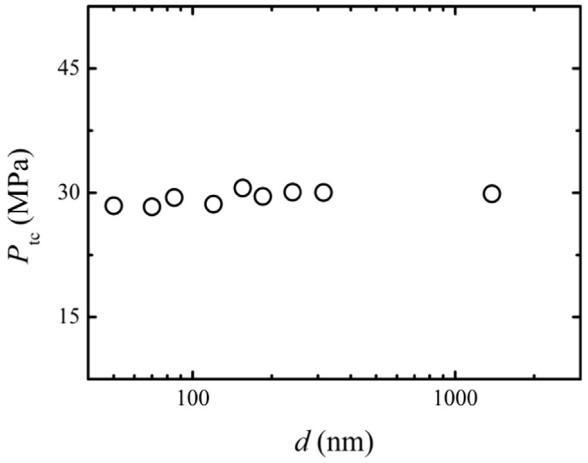

Fig. 6. The transmitted-wave pressure, P_{tc}, as a function of the average pore size, d.

the peak pressure in the wave profile) of silica nanofoams with different average pore sizes were summarized in Table 2 and Fig. 8.

2.2.5. Quantitative SEM image analysis

After testing, the dynamically sheared silica samples were well preserved. Selected samples were cleaved along the radius direction (Fig. 9a), and the areas around the circular bands of shear deformation in the exposed lateral surfaces, as depicted by the dashed rectangular box in Fig. 9b, were observed under a FEI-XL30 environmental scanning electron microscope (SEM) at 20 kV, with the spot size of 3.0. The SEM samples had been coated with iridium using an Emitech K575X sputter coater at 85 mA for 6 s prior to the observation. Fig. 9c shows typical SEM images. The porous structures near and far away from the edge of incident bar were observed at different magnifications, as shown in Fig. 9d.

A quantitative SEM image analysis algorithm was developed to determine the boundaries of SDZ. Outside the SDZ, no permanent cell deformation could be detected. Inside the SDZ, the porosity changed significantly. Details of this technique has been documented in Appendix C. As shown in Fig. 10, image filtering [48] was first conducted to enhance the local contrast of the original SEM image. Then, the enhanced image was converted into binary format, where the Otsu's method [49] was used to obtain the threshold. On the converted image, a nominal two-dimensional porosity, p_2, was defined as the fraction of the black area. The p_2 value of the far field was employed as the reference. For self-comparison purpose, SDZ was defined as the area where the local porosity differs from that in far field by more than ~1 σ_s, with σ_s being the standard deviation. The image analysis results are shown in Fig. 11, with the solid lines marking out the SDZ boundaries.

3. Results and discussion

As shown in Fig. 1e, the testing specimens are in the disk form having the diameter of ~23 mm and the thickness of 4.50 mm. The porosities of all the foam silica are around 60%; their pore sizes ranges from dozens of nm to more than 1 μm, with relatively narrow pore size distributions. In Fig. 1a, through x-ray diffraction (XRD) analysis, it is confirmed that all the samples were in the same amorphous silica phase [50]. Fig. 1(b–d) shows the porous

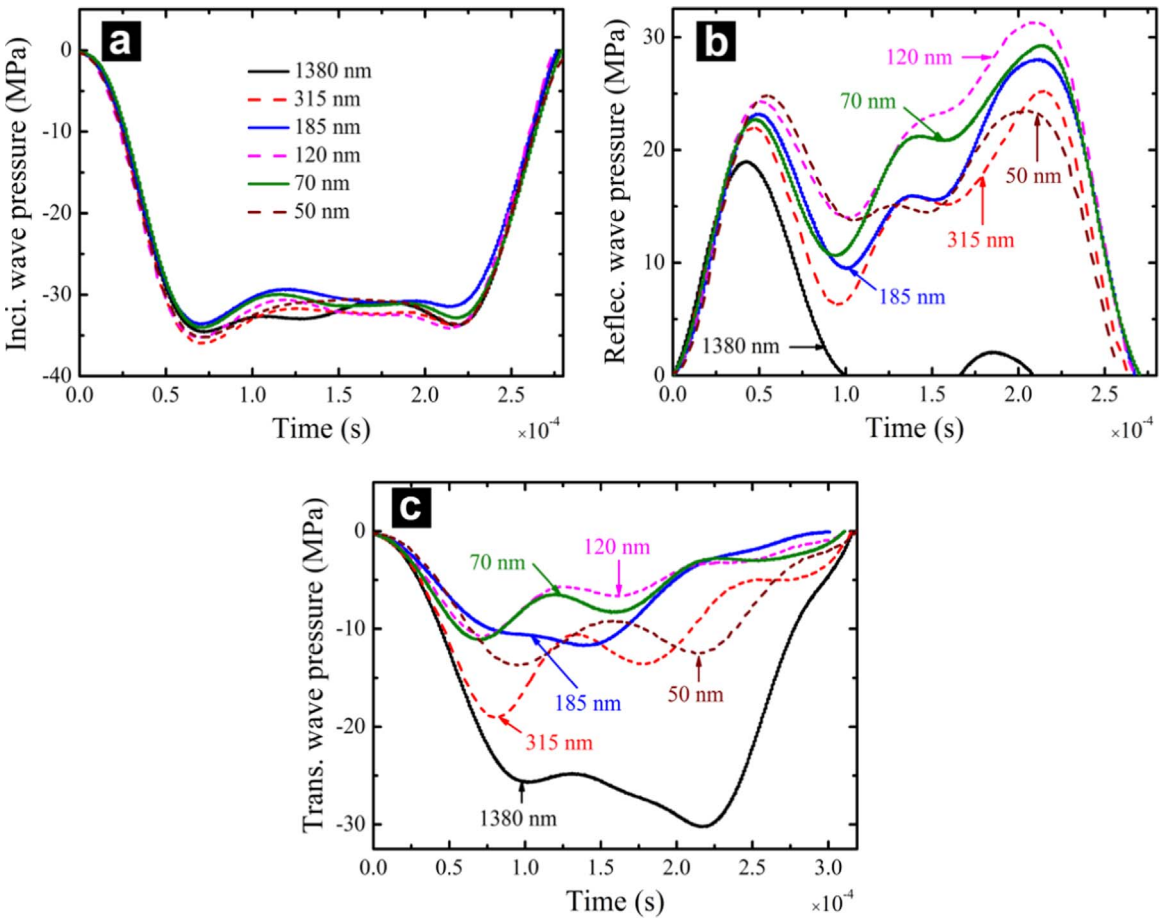

Fig. 7. Typical profiles of (a) incident, (b) reflected, and (c) transmitted stress waves under dynamic shear conditions. The arrows indicate the average pore sizes of silica foams. The impact rate of striker is ~8.5 m/s.

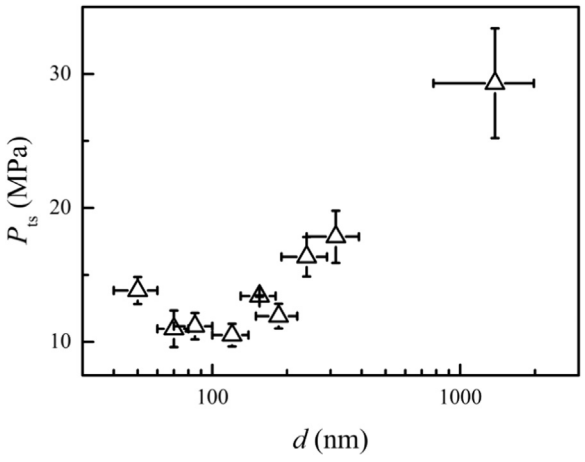

Fig. 8. The transmitted-wave pressure, P_{ts}, as a function of the average pore size, d.

morphology. The pores are random, interconnected and of similar shapes.

As shown in Fig. 3, the quasi-static peak shear stresses are similar for all the foam samples. The results in Table 2 and Fig. 4 suggest that the quasi-static shear strength, S_0, is quite insensitive to the pore size, as predicted by the classic theory [32]: The strength/hardness and toughness of a foam material are determined by its porosity, p.

$$S_0 \propto (1-p)^{\delta} \tag{3}$$

where δ is a system constant. Since all the silica foam disks in the current study have a similar porosity, ~60%, their quasi-static shear strengths are at the same level, ~11.1 MPa.

In the dynamic SHB tests, because the striker speed is kept nearly constant (~8.5 m/s), the incident-wave profiles and pressures are similar for all the samples, as shown in Table 2. With the incident-wave pressure of ~31 MPa, in the dynamic compression test, the cell deformation is quite elastic; while in the dynamic shear tests, the pores collapse (Fig. 9d), and the stress wave is highly nonlinear. The acoustic impedance (z) of silica foam is determined by [51]

$$z = A \bullet \rho \bullet c \tag{4}$$

where A is the cross sectional area, ρ is the mass density, and c is the speed of sound, all of which are unrelated to the pore size, d. Thus, the acoustic impedances of all the silica foams should be similar. The stress wave in the incident bar is one-dimensional and its wave front is regular, i.e. homogeneous along transverse directions [47]. When such a one-dimensional stress wave encounters an interface, a part of it will be reflected, determined by the impedance mismatch. As shown in Table 2 and Fig. 6, the transmitted-wave pressure is nearly constant for all the silica foams, independent of the pore size, indicating that, under compressive stress waves, the acoustic impedance and the wave propagation of silica foams are not related to d, as predicted by classic dynamic mechanics theory [52,53].

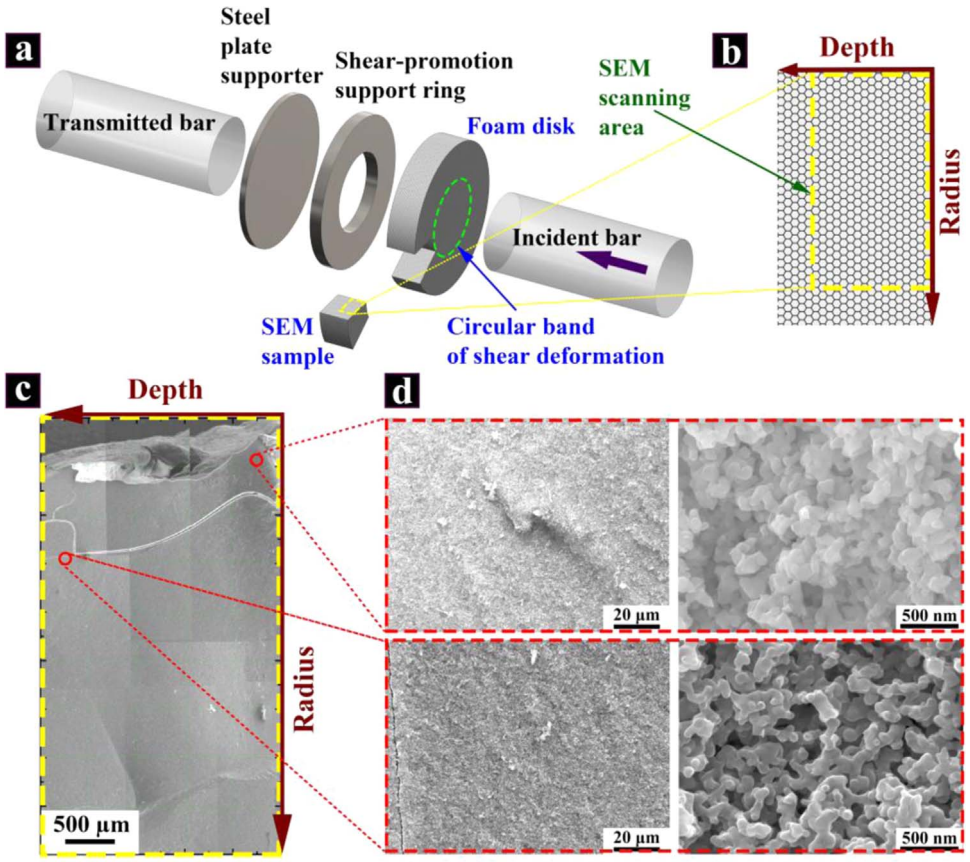

Fig. 9. Schematics of (a) the SHB experimental setup for the dynamic shear test, and (b) the scanning area (the dashed rectangle) in a SEM sample harvested from a tested silica foam disk. (c) A typical SEM image of the dynamically sheared silica nanofoam sample. (d) Porous structures in the shear deformation zone (top row) and in the far field (bottom row) of a tested nanofoam sample.

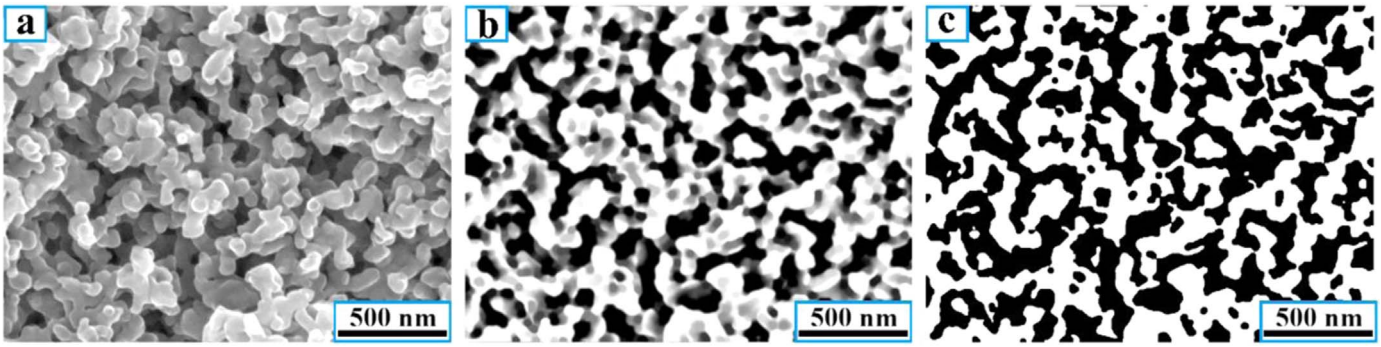

Fig. 10. The filtering technique for the quantitative image analysis: (a) an original SEM image; (b) an enhanced SEM image using the Shading Correction and the Local Equalization techniques; (c) a binary SEM image using the Otsu method.

In the dynamic shear experiment, while the stress wave in the incident bar was compressive, shear deformation was promoted in the narrow circular band in-between the outer surface of incident bar and the inner surface of SPSR. Due to the geometrical change, the stress wave in the silica sample was no longer homogeneous, but localized; i.e. its spatial distribution is nonuniform. Under this condition, as shown in Table 2 and Fig. 8, the transmitted-wave pressure becomes highly dependent on the pore size. As the pore size decreases from ~1.4 μm to ~300 nm, the transmitted-wave pressure is lowered relatively slowly by nearly ~30%; as the pore size further decreases to ~100 nm, the transmitted-wave pressure rapidly reduces by another ~30%. Overall, with the pore size around 100–200 nm, the transmitted-wave pressure is only ~1/3 of that of the large-pore-sized samples. In our experiment, the incident-wave pressure and duration are maintained at constant levels; as the impedance of the material is unrelated to the pore size, the reflected-wave profiles do not have any correlation with the pore size. The trend in transmitted waves must be associated with the structural changes and the energy absorption of the foams.

As shown in Fig. 11, when the pore size, d, decreases from above 300 nm to ~100 nm, the SDZ configuration undergoes a sharp transition. When $d > 300$ nm, the stress wave in the silica foams exhibits typical concentrated characteristics. The shear deformation is localized in the narrow circular band between the outer surface of incident bar and the inner surface of SPSR. When d is ~100–200 nm, the SDZ size abruptly increases. A much broader field of material is involved in the wave propagation and pore collapse, leading to a much larger volume of structural variation, V; that is, the localized stress wave is homogenized and

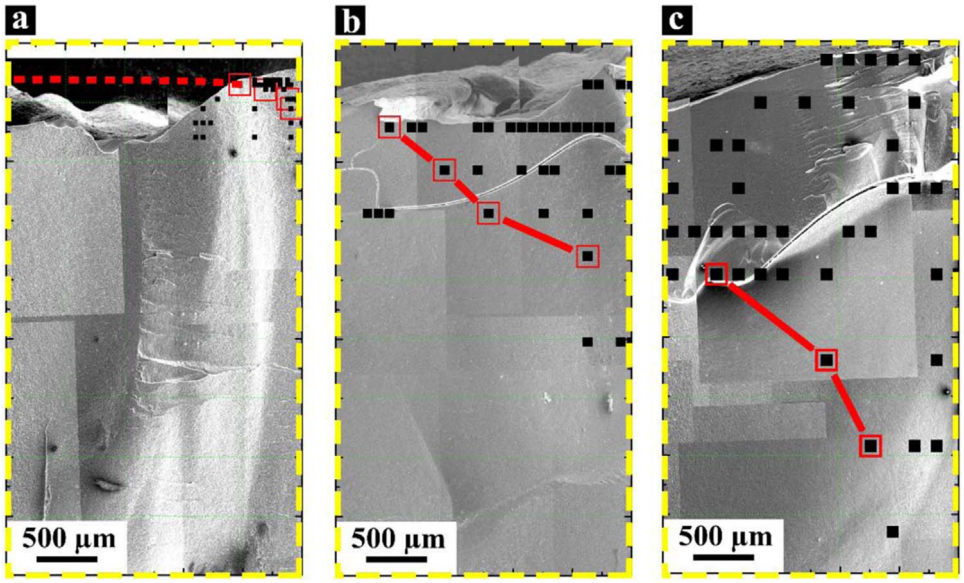

Fig. 11. SEM images of tested silica nanofoams with the average pore sizes of (c) 315 nm, (d) 155 nm, and (e) 120 nm, respectively. The solid squares indicate the local areas where nanopores are highly deformed; the solid lines show the boundaries of shear deformation zones (SDZ).

widespread energy absorption is promoted. Because more wave energy is dissipated, the transmitted-wave pressure decreases with the pore size.

The classic Grady's model, Eq. (1), does not account for any size effect [25,27–31], which is against our observation in silica nanofoams. However, it does provide a framework to collectively analyze the physical parameters [1]. With the pore size (d) being a variable, the SDZ size (w) can be expressed as

$$w = f(K_c, \rho, C, \dot{\varepsilon}, d) \tag{5}$$

where f is a certain function. According to the Π theorem [54],

$$w/d = f\left(\frac{K_c}{\rho C \dot{\varepsilon} d^{3/2}}\right) \tag{6}$$

If f is set to a power law form, Eq. (6) becomes

$$w/d = \alpha\left(\frac{K_c}{\rho C \dot{\varepsilon} d^{3/2}}\right)^{\chi} \tag{7}$$

where α and $\chi \geq 2/3$ are two dimensionless material parameters. Eq. (7) can be rewritten as

$$w = \alpha\left(\frac{K_c}{\rho C \dot{\varepsilon}}\right)^{\chi} \cdot d^{1-3\chi/2} \tag{8}$$

When $\chi = 2/3$, Eq. (8) is reduced to Eq. (1) and w is independent of d. If $\chi > 2/3$, the SDZ size, w, increases as the pore size, d, decreases, agreeing with our experimental observation. For the silica nanofoams under investigation, as shown in Fig. 11, the SDZ size was measured from the SEM image as the area surrounded by the solid lines, and was averaged over the sample thickness. In Fig. 12, through data fitting, the value of χ is determined as 2.1 ± 0.1, or ~ 2.0; hence, $w \propto 1/d^{2}$. When the pore size is relatively large, e.g. larger than 300 nm, the SDZ size converges to the shear gap width of 0.2 mm.

The capacity of energy dissipation of a silica foam may be described by the energy dissipation factor (β):

$$\beta = \frac{U_i - U_r - U_t}{U_i - U_r} \tag{9}$$

where U_i, U_r, and U_t are the energies carried by the incident,

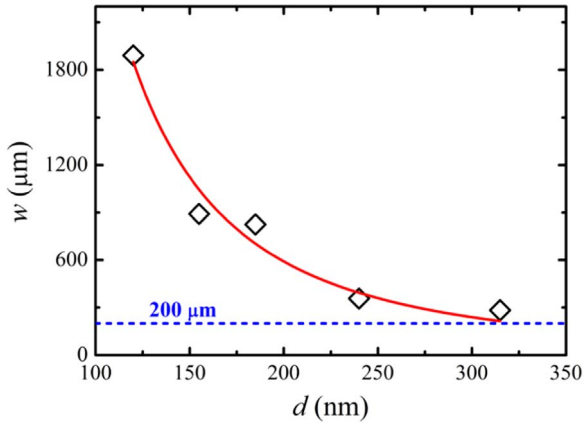

Fig. 12. The average shear-deformation-zone (SDZ) size, w, as a function of the average pore size, d, fitted with the power law, w ∝ d1–3χ/2. The diamonds show the testing data; the solid line is the regressed curve; the dashed line indicates the shear-gap width (200 μm) between the incident bar and the SPSR.

reflected, and transmitted waves, respectively. When a linear, one-dimensional stress wave propagates in an elastic medium, the stress wave energy (U) consists of two parts: the strain energy (U_s) associated with local deformation and the kinetic energy (U_k) associated with local particle velocity. The strain energy may be assessed as

$$U_s = A_b C_b / (2E_b) \cdot \int_0^{T_P} P_w^2 dt, \tag{10}$$

where A_b, C_b, E_b, P_w, and t are the cross-sectional area of the medium, the speed of sound, the Young's modulus of the medium, the wave pressure, and the time, respectively [55,56]. The integration is performed over the pulse duration, T_P. The kinetic energy can be estimated as

$$U_k = \rho_b A_b C_b^3 / (2E_b^2) \cdot \int_0^{T_P} P_w^2 dt, \tag{11}$$

where ρ_b is the mass density. Thus, the stress wave energy (U)

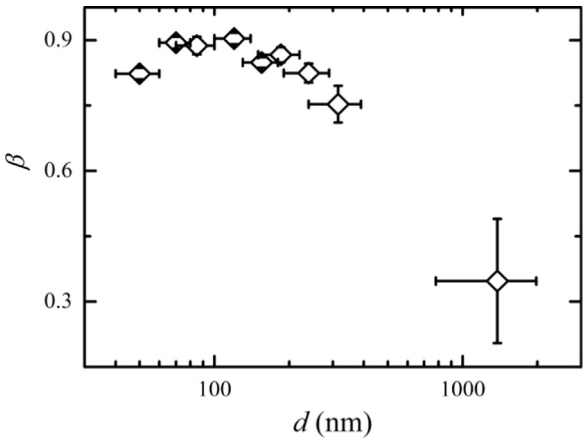

Fig. 13. The energy dissipation factor, β, as a function of the average pore size, d.

$$U = U_s + U_k = \left(\frac{A_b C_b}{2E_b} + \frac{\rho_b A_b C_b^3}{2E_b^2}\right)\cdot \int_0^{T_P} P_w^2 dt = \xi \cdot \int_0^{T_P} P_w^2 dt \quad (12)$$

where $\xi = A_b C_b/(2E_b) + \rho_b A_b C_b^3/(2E_b^2)$. For a linear elastic medium, $E_b = \rho_b C_b^2$; hence, $\xi = A_b C_b/E_b$. For the Split Hopkinson Bar (SHB) system used in the current investigation, $A_b = 126.7\ mm^2$; $C_b = 5790$ m/s; $E_b = 196.5$ GPa. Therefore, the system constant $\xi = 3.73 \times 10^{-12}\ m^5N/s$. Here, the definition of stress wave energy is only for self-comparison purpose.

The calculation results of the energy dissipation factor, β, are summarized in Table 2 and Fig. 13. With a relatively large pore size above 1 μm, the energy dissipation is quite low; as the pore size decreases, β rapidly increases, and reaches the peak value as d is ~100 nm, consistent with the observed SDZ configurations.

The wave homogenization in small-pore-sized silica nanofoams should be attributed to the fast condensation caused by cell deformation. When a stress wave encounters a hard inclusion, its front may be dispersed to a broader field [18]. In the silica nanofoams under investigation, initially the materials are uniform. As the intense localized stress wave advances, pore collapse occurs. When the pore size is relatively large, e.g. comparable with or larger than the characteristic size of wave front, pore collapse leads to local "softening", which promotes wave instability [57,58], so that the stress wave is concentrated in the gap between the incident bar and the SPSR. When the pores are relatively small, e.g. much smaller than the characteristic size of wave front, their collapse takes only a short period of time and effectively becomes a local compaction/hardening process. Therefore, shear concentration is suppressed, and the wave front is dispersed into far field.

In the dynamic shear test, the broadening of intense stress wave is evident only when the pore size is sufficiently small. To identify the critical condition where the wave broadening starts, we define the pressure reduction factor (ς)

$$|\varsigma| = |P_{ts} - P_{t0}|/P_{t0} \quad (13)$$

where P_{t0} is the equivalent maximum normal stress under quasi-static shear condition. For the silica nanofoams with the porosity of ~60%, the measured P_{t0} is ~16.1 MPa. When $\varsigma > 0$ (ς^+), the maximum transmitted-wave pressure is higher than 16.1 MPa, and this region is defined as the Regular Region; when $\varsigma < 0$ (ς^-), the maximum transmitted-wave pressure is lower than 16.1 MPa, and this region is defined as the Nano Region. The boundary between the Regular Region and the Nano Region, ~200 nm, defines the point where the localized stress wave starts to be homogenized.

4. Conclusions

According to conventional theory, pore size has little influence on the quasi-static shear strength of a foam. In the current study, we show that when a silica foam is subjected to an intense shear stress wave and its pore size is less than 200 nm, a strong size effect can be observed: The smaller the pores, the broader the shear-deformation zone is and the more energy the silica foam absorbs. That is, as the pore size is reduced to the nanometer scale, silica nanofoam suppresses shear localization and promotes bulk-distributed energy absorption. We attribute this size effect to the fast condensation of the nanopores at the stress wave front. As the pore size is smaller than the characterize lengths of wave front and typical shear deformation zone, and the pore collapse time is shorter than the characteristic time of wave propagation, pore collapse effectively leads to local hardening and disperses the intense stress wave to a broader field. Thus, a large volume of material is involved in energy absorption and the transmitted-wave pressure is much reduced. The classic Grady's equation is modified to capture the pore size effect; the shear-deformation-zone size approximately follows an inverse-square law of the pore size. The presence of the Nano Region of foam materials may open a door to mitigation of intense stress waves and promotion of energy absorption.

Acknowledgements

This research was supported by The Army Research Office under Grant No. W911NF-12-1-0011, for which the authors are grateful to Dr. David M. Stepp. Special thanks are also due to Professors Jian Luo, Vitali F. Nesterenko and Marc A. Meyers for the useful discussions.

Appendix A. Sample processing and characterization

A.1. Sol-gel methods

Silica monoliths with various pore sizes were synthesized through sol-gel method, following the works of [42] for silica samples with the average pore size smaller than 500 nm, and [39,41] for silica samples with larger average pore sizes, respectively.

For the former (smaller pores), Sigma-Aldrich Ludox HS-40 colloidal silica was mixed with PQ Kasil-1 potassium silicate solution in a flask, by magnetic stirring for 30 min. The total mass was 800 g. The mass ratio was in the range from 1:99 to 40:60. A larger colloidal silica amount would lead to a smaller pore size. With the silica-silicate mixture being vigorously stirred, 200 g formamide solution (40 wt% formamide and 60 wt% deionized water) was slowly added in, and the stirring continued for 30 min, by using a magnetic stirrer. Then the solution was transported into a polypropylene plastic vial with the inner diameter of 35.6 mm and the height of 16.3 mm. After aging at room temperature for 24 h, the wet gels were rinsed first by 1 M ammonium nitrate, then by 1 M nitric acid, then by deionized water at about 90 °C, and finally by pure methanol at room temperature.

For the latter (larger pores), 28 g Sigma-Aldrich polyethylene glycol (PEG, with the average molecular weight of 10,000) was first dissolved in 300 ml 0.01 M acetic acid aqueous solution. Then, 150 ml Sigma-Aldrich tetramethyl orthosilicate (TMOS, 98%) was added and thoroughly mixed by a magnetic stirrer in a flask for 30 min. The mixture was transported into a polypropylene plastic vial with the inner diameter of 46.2 mm and the height of

Table A1
Effects of SCC temperature on the porosity and the pore size.

Sample No.	Temperature (°C)	Porosity	Pore size (nm)
#03	850	85.6%	210 ± 67
#03	1250	55.1%	159 ± 70
#07	850	83.8%	132 ± 49
#07	1250	65.8%	106 ± 41
#10	850	79.9%	41 ± 3
#10	1150	78.1%	44 ± 2
#10	1200	76.0%	45 ± 7
#10	1250	65.5%	46 ± 9

21.6 mm. After aging at 40 °C for 72 h, the gels were washed sequentially by 0.1 M aqueous ammonia solution at about 120 °C, 0.1 M nitric acid and deionized water at about 90 °C, and finally pure methanol at room temperature.

In both methods, each step of the rinsing process was repeated for more than five times. After rinsing, the silica monolith was thermally treated in a VWR 1330GM oven at 80 °C for 72 h.

A.2. Subcritical calcination

The obtained silica monoliths had different average pore sizes and porosities. The pore size and the porosity were highly correlated. In order to uncouple these two important parameters, specifically to vary the pore size in a broad range and keep the porosity around 60%, a subcritical calcination (SCC) treatment was carried out in a MTI GSL-1700X horizontal tube furnace at selected temperatures (T_s) for 1 h. The SCC temperatures ranged from 850 °C to 1265 °C. The ramp rate was initially set as 3 °C/min; and when the temperature was less than 100 °C away from T_s, was reduced to 1 °C/min. In order to minimize the residual stress, the cooling rate was set to be 3 °C/min. More details have been documented elsewhere [43].

As shown in Table A1, compared with the pore size, the porosity was much more sensitive to the SCC temperature [43]. As the SCC temperatures were optimized for silica monoliths of various initial pore sizes, their porosities could be adjusted to a similar level, ~60% while their pore sizes ranged from ~50 nm to ~1400 nm, as shown in Table 1 in the main text.

A.3. Surface conditioning

The SCC-treated silica monoliths were surface polished by a set of silicon carbide sandpapers [59,60], starting from 320-grit ones, followed by 600-grit, 1200-grit, and finally 2500-grit sandpapers. The initial sample thickness before SCC treatment was 10–14 mm, and 8–9 mm after the treatment. The sample thickness after each step of sandpaper polishing was 5–6 mm, 5 mm, 4.75 mm, and 4.50 mm, respectively. The tolerance of final thickness was ± 50 μm.

A.4. Porosity

The porosity of a silica nanofoam sample, p, was calculated from its mass density, ρ [32]: $p=1-\rho/\rho_s$, where $\rho_s=2.2$ g/cm^3 is the density of solid amorphous silica [61]. The mass density was the mass of the disk sample divided by its volume [43].

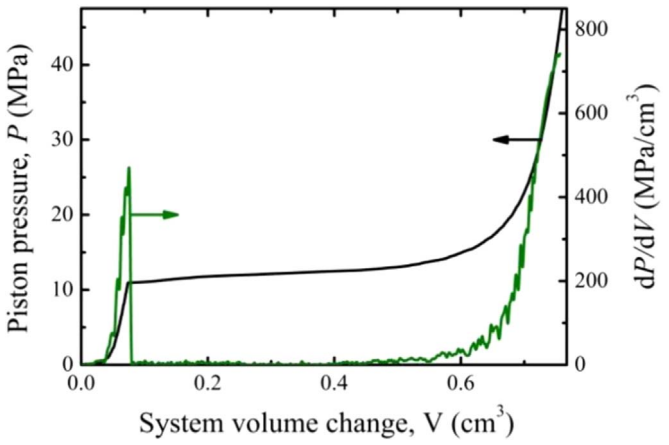

Fig. A1. Typical curves of mercury porosimetry. The black line (left) is a sorption isotherm curve. The olive line (right) is dP/dV.

A.5. Pore size

The pore size was evaluated by the Washburn equation [62]: $d=4\sigma\cdot\cos\theta/P_{Hg}$, where $\theta\sim140°$ is the contact angle, $\sigma=0.484$ N/m the surface tension of mercury, and P_{Hg} the mercury infiltration pressure. The mercury porosimetry analysis was conducted by immersing a silica nanofoam sample with the mass of 0.5–1.5 g into mercury in a stainless steel cylinder. The inner diameter of the cylinder was 19.05 mm. The top of the cylinder was sealed with a steel piston and a Buna-N o-ring. On an Instron 5582 machine, at the rate of 0.10 mm/min, the piston was compressed into the cylinder. The piston displacement and piston force were recorded. The change of the system volume, V, was obtained by multiplying the piston displacement with the piston cross-sectional area. The piston pressure, P, was calculated via dividing the piston force by the piston cross-sectional area. In Fig. A1, the first order derivation of dP/dV was used to determine the range of the infiltration plateau. The lower limit was taken as the point where dP/dV abruptly dropped; the upper limit was set as the point where dP/dV started to depart from zero. The average pore size was taken as the middle point between the minimum and the maximum pore sizes calculated from the infiltration plateau.

A.6. Powder x-ray diffraction

The SCC-treated silica nanofoams were characterized by a Bruker D8 Advance Diffractometer using Cu Kα radiation ($\lambda=1.5418$ Å), with the scan speed of 0.1 s/step, the step size of 0.02°, the 2θ range of 10–80°. Fig. 1a in the main text shows typical x-ray diffraction curves of silica nanofoams.

A.7. SEM image analysis

The silica nanofoams were observed under a FEI-XL30 environmental scanning electron microscope (SEM) at 20 kV, with a spot size of 3.0. The SEM samples had been coated with iridium using an Emitech K575X sputter coater at 85 mA for 6 s prior to the observation. The porous configurations of the samples with different average pore sizes were shown in Fig. 1(b–d) in the main text, with the same scale bar of 500 nm. Take the sample with the average pore size of ~315 nm as an example, Fig. A2 shows the porous structure at different magnifications.

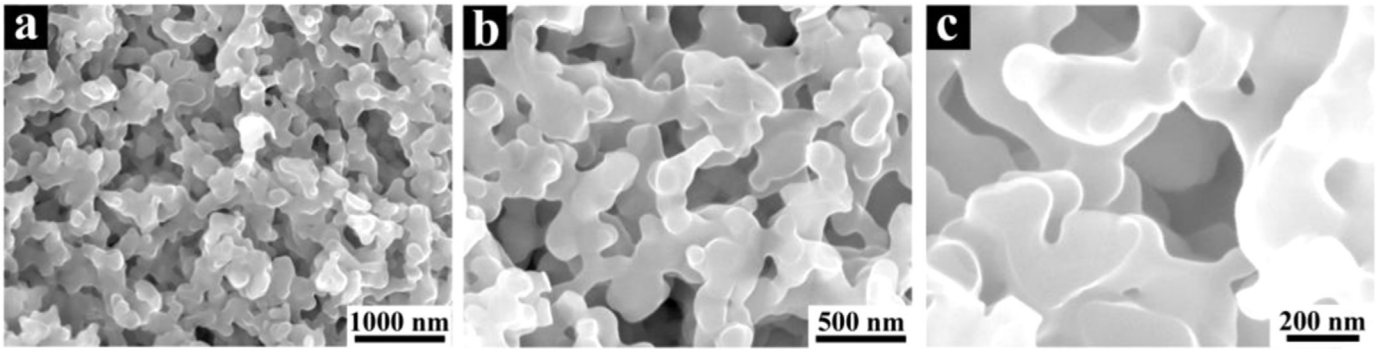

Fig. A2. SEM images of a silica nanofoam sample with the average pore size of 315 nm at different magnifications.

Appendix B. The Split Hopkinson Bar (SHB) system

The dynamic responses of silica nanofoams were characterized by a Split Hopkinson Bar (SHB) system [47], as shown in Fig. B1. By using a gas chamber, a Grade 9 titanium (Ti) tube striker was projected onto the near end of a stainless steel incident bar. The outer diameter, the inner diameter, and the length of the striker were respectively 12.7 mm, 11.4 mm, and 462.0 mm. The two ends of the Ti tube were sealed by two 17–4 PH H900 stainless steel endcaps, respectively. The endcaps were pressed into the tube with a tight fit, and fixed by two stainless steel pins across the tube wall, respectively. The thickness of the endcaps was 5.1 mm, and the pin diameter and length were 3.2 mm and 12.7 mm, respectively. The total mass of the striker was 62.8 g. The striker was hosted by an AeroMarine polyurethane foam sleeve inside the gas chamber. The inner pressure in the gas chamber was fixed at 15.0 psi, leading to a nearly constant striker speed of 8.5 m/s. The striker speed was measured by a couple of OMRON EE-SPW421 photomicro sensors.

The diameters of the incident bar and the transmission bar were the same, $D=12.7$ mm; the lengths of them were 178 cm and 152 cm, respectively. They were made of 17–4 PH H900 stainless steel. The Young's modulus was 196.5 GPa, and the density was 7750 kg/cm^3. Two sets of Vishay WK-13-250BF-10C strain gauges were mounted on the centers of the two bars, respectively, so as to measure the profiles of stress waves, through a Vishay 2310B data acquisition system (DAS).

To ensure that only a single pulse loading would be applied on the silica nanofoam sample, a momentum trapper was employed, following the works of [45,46], as shown in Fig. B1c. It consisted of a stiff block, a flange attached to the near end of the incident bar, and a two-piece thread clamping locknut. There was a gap

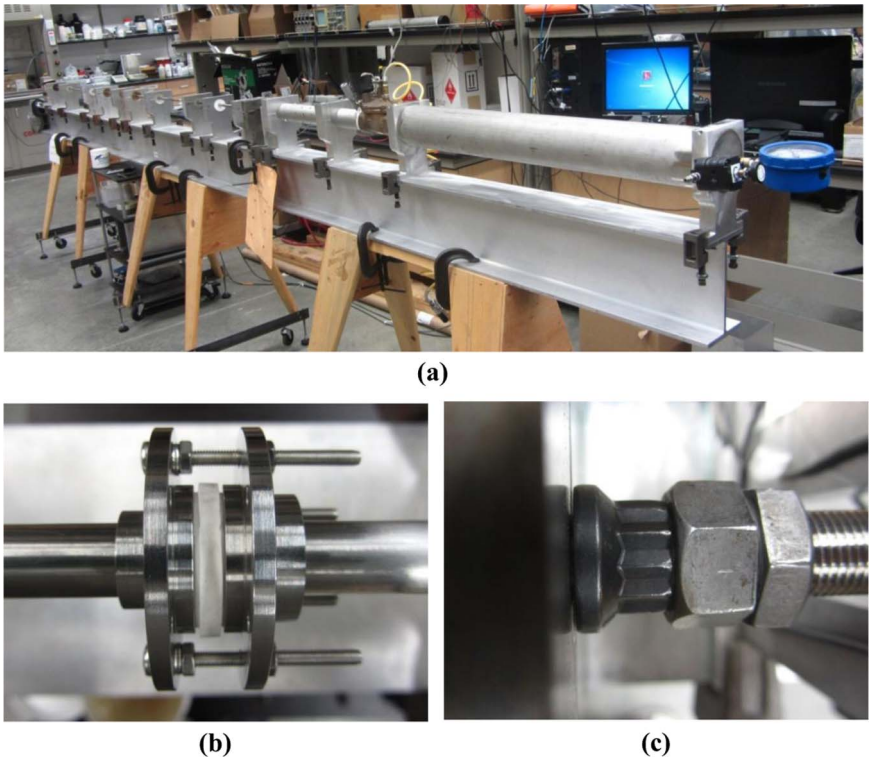

Fig. B1. The Split Hopkinson Bar (SHB) system: (a) the system configuration; (b) the shear-promotion support ring (SPSR); and (c) the momentum trapper.

between the flange and the rigid block. The gap width was precisely controlled so that the motion of the flange would be stopped immediately after the tensile stress wave generated by the striker had entered into the incident bar. Thus, repeated pulse loading was prevented.

Appendix C. Quantitative image analysis

The silica nanofoam disks tested in the dynamic shear experiment were well preserved for further examination. After testing, a SEM sample was harvested from the disk, and the area around shear deformation zone in the exposed lateral surface was observed by a FEI-XL30 environmental scanning electron microscope (SEM).

Because the depth of the SEM view field was larger than the pore size, there would inevitably be shadows in the SEM images. In order to carry out a quantitative image analysis, image filtering was conducted through a combination of the Shading Correction technique developed by Reyes-Aldasoro [48] and the Local Equalization function provided by the Image-Pro Plus software (Media Cybernetics Manufacturing, Warrendale, PA, USA), as demonstrated in Fig. 10 in the main text. A SEM image was first enhanced by the Shading Correction, reducing the shadow of the porous structure. Then it was imported into Image-Pro Plus, and Local Equalization was employed to enhance its local contrast with the window size of 60 pixels, the step of 1 pixel, and the standard deviation of 0.5. Finally the Otsu's method [49] was used to obtain the threshold (Matlab built-in function Graythresh) and the image was converted into binary format. On the converted image, a nominal two-dimensional porosity, p_2, was defined as the fraction of the black area. The measurement results of p_2 qualitatively matched the porosity data calculated from mass density (p) for untested silica nanofoams, quite acceptable for self-comparison purpose. The numbers of pixels in white and black areas were counted through the Matlab built-in function Bwarea.

SEM images of an exposed inner surface were placed together to construct an overall map. The map was divided into a large number of small grids, and for each grid the value of local nominal two-dimensional porosity, p_2, was calculated. The grid was rectangular, with the size of $93m$ μm by $242n$ μm, where m and n are positive integers. Typically, a 2500 μm by 4500 μm area surrounding the shear deformation zone was scanned. The scanning area covered more than one half of the sample thickness. The scanning was along 5 or 6 straight lines parallel to the sample depth direction; along each line about 20 points were scanned; and around each point about 6 SEM images were taken. Cracked areas were skipped.

For each pore size, a reference nominal two-dimensional porosity, p_2^*, was measured from a pristine nanofoam sample. As the sample was quite homogeneous and the number of pores was large, across an exposed inner surface, the standard deviation of p_2^* was less than 2% of its average value. The results are shown in Table C1.

For a dynamically sheared sample, if the local value of p_2 was different from p_2^* by more than $\sim 1\ \sigma_s$, with σ_s being the standard deviation, the pores in the grid was regarded as being damaged. The image analysis results were shown in Fig. 11 in the main text, with the black squares indicating the local areas of deformed porous structures and the lines marking out the boundaries of shear deformation zones.

Table C1
Image analysis results of pristine silica nanofoams.

d (nm)	315 ± 75	240 ± 50	185 ± 35	155 ± 25	120 ± 20	85 ± 15
p (%)	63.0	62.1	62.9	60.6	63.5	62.4
p_2^* (%)	52.4 ± 0.8	50.8 ± 1.0	50.7 ± 1.3	50.4 ± 0.6	52.4 ± 0.8	50.4 ± 0.8

References

[1] V.F. Nesterenko, Dynamics of Heterogeneous Materials, Springer Science & Business Media, New York, NY, 2001.
[2] M.A. Meyers, Dynamic Behavior of Materials, John Wiley & Sons, Somerset, NJ, 1994.
[3] M.A. Meyers, G. Subhash, B.K. Kad, L. Prasad, Mech. Mater. 17 (1994) 175–193.
[4] Y. Me-Bar, D. Shechtman, Mater. Sci. Eng. 58 (1983) 181–188.
[5] S.P. Timothy, I.M. Hutchings, Acta Metall. 33 (1985) 667–676.
[6] Q. Xue, M. Meyers, V. Nesterenko, Acta Mater. 50 (2002) 575–596.
[7] P. Longère, A. Dragon, Mech. Mater. Part B 80 (2015) 203–218.
[8] D.K. Balch, J.G. O'Dwyer, G.R. Davis, C.M. Cady, G.T. Gray, D.C. Dunand, Mater. Sci. Eng.: A 391 (2005) 408–417.
[9] R. Tounsi, E. Markiewicz, G. Haugou, F. Chaari, B. Zouari, Int. J. Solids Struct. 80 (2016) 501–511.
[10] M.A. Meyers, V.F. Nesterenko, J.C. LaSalvia, Q. Xue, Mater. Sci. Eng.: A 317 (2001) 204–225.
[11] C. Daraio, V.F. Nesterenko, E.B. Herbold, S. Jin, Phys. Rev. Lett. 96 (2006) 058002.
[12] S. Pauly, S. Gorantla, G. Wang, U. Kühn, J. Eckert, Nat. Mater. 9 (2010) 473–477.
[13] R.O. Ritchie, Nat. Mater. 10 (2011) 817–822.
[14] C. Zener, J.H. Hollomon, J. Appl. Phys. 15 (1944) 22–32.
[15] M. Zhou, A. Rosakis, G. Ravichandran, J. Mech. Phys. Solids 44 (1996) 981–1006.
[16] Y. Xu, J. Zhang, Y. Bai, M.A. Meyers, Metall. Mater. Trans. A 39 (2008) 811–843.
[17] M.A. Porter, C. Daraio, I. Szelengowicz, E.B. Herbold, P. Kevrekidis, Physica D: Nonlinear Phenom. 238 (2009) 666–676.
[18] A. Leonard, C. Daraio, Phys. Rev. Lett. 108 (2012) 214301.
[19] V.F. Nesterenko, C. Daraio, E.B. Herbold, S. Jin, Phys. Rev. Lett. 95 (2005) 158702.
[20] Y. Starosvetsky, A.F. Vakakis, Phys. Rev. E 82 (2010) 026603.
[21] G. Theocharis, N. Boechler, P.G. Kevrekidis, S. Job, M.A. Porter, C. Daraio, Phys. Rev. E 82 (2010) 056604.
[22] E. Pekarskaya, C. Kim, W. Johnson, J. Mater. Res. 16 (2001) 2513–2518.
[23] V. Nesterenko, M. Meyers, H. Chen, Acta Mater. 44 (1996) 2017–2026.
[24] K.A. Alshibli, S. Sture, J. Comput. Civ. Eng. 13 (1999) 103–109.
[25] D. Grady, J. Appl. Phys. 53 (1982) 322–325.
[26] D.E. Grady, M.E. Kipp, Int. J. Rock Mech. Min. Sci. Geomech. Abstr. (1980) 147–157.
[27] C. Shih, M. Meyers, V. Nesterenko, Acta Mater. 46 (1998) 4037–4065.
[28] C. Shih, V. Nesterenko, M. Meyers, J. Appl. Phys. 83 (1998) 4660–4671.
[29] V.F. Nesterenko, P.-H. Chiu, C. Braithwaite, A. Collins, D.M. Williamson, K.L. Olney, D. Benson, F. McKenzie, M.L. Elert, W.T. Buttler, AIP Conference Proceedings-American Institute of Physics, 2012, p. 533.
[30] P. Forquin, F. Hild, A. Probabilistic, Damage model of the dynamic fragmentation process in brittle materials, in: A. Hassan, G. Erik van der (Eds.), Advances in Applied Mechanics, Elsevier, Cambridge, MA, 2010, pp. 1–72.
[31] P. Perzyna, Int. J. Solids Struct. 22 (1986) 797–818.
[32] L.J. Gibson, M.F. Ashby, Cellular Solids: Structure and Properties, Cambridge University Press, London, UK, 1997.
[33] L.J. Gibson, J. Biomech. 38 (2005) 377–399.
[34] P. Fratzl, R. Weinkamer, Prog. Mater. Sci. 52 (2007) 1263–1334.
[35] M. Borrega, L.J. Gibson, Mech. Mater. 84 (2015) 75–90.
[36] R.H. Baughman, A.A. Zakhidov, W.A. de Heer, Science 297 (2002) 787–792.
[37] J.L. Hedrick, K.R. Carter, J.W. Labadie, R.D. Miller, W. Volksen, C.J. Hawker, D. Y. Yoon, T.P. Russell, J.E. McGrath, R.M. Briber, Nanoporous polyimides, in: H. R. Kricheldorf (Ed.), Progress in Polyimide Chemistry II, Springer Berlin Heidelberg, Springer, Heidelberg, Germany, 1999, pp. 1–43.
[38] B.C. Tappan, S.A. Steiner, E.P. Luther, Angew. Chem. Int. Ed. 49 (2010) 4544–4565.
[39] K. Nakanishi, Synthesis Concepts and Preparation of Silica Monoliths, Monolithic Silicas in Separation Science: Concepts, Syntheses, Characterization, Modeling and Applications, John Wiley & Sons, Somerset, NJ 2010, p. 11.
[40] M. Scheffler, P. Colombo, Cellular Ceramics: Structure, Manufacturing, Properties and Applications, John Wiley & Sons, Somerset, NJ, 2006.
[41] R. Miyamoto, Y. Ando, C. Kurusu, Hz Bai, K. Nakanishi, M. Ippommatsu, J. Sep. Sci. 36 (2013) 1890–1896.
[42] R.D. Shoup, Controlled pore silica bodies gelled from silica sol-alkali silicate mixtures, in: M. Kerker (Ed.), Colloid and Interface Science, Academic Press, New York, 1976, pp. 63–69.
[43] C. Zhao, M. Wang, Y. Shi, J. Cao, Y. Qiao, Mater. Des. 90 (2016) 815–819.
[44] M.A. Meyers, L.E. Murr, K.P. Staudhammer, Shock-Wave and High-Strain-Rate Phenomena in Materials, CRC, CRC Press, Boca Raton, FL, 1992.
[45] B. Song, W. Chen, Exp. Mech. 44 (2004) 622–627.
[46] S. Nemat-Nasser, J.B. Isaacs, J.E. Starrett, Proc. R. Soc. Lond. Ser. A: Math. Phys. Sci. 435 (1991) 371–391.
[47] H. Kolsky, Stress Waves in Solids, Courier Corporation, North Chelmsford, MA, 1963.
[48] C.C. Reyes-Aldasoro, Electron. Lett. 45 (2009) 454–456.
[49] N. Otsu, Automatica 11 (1975) 23–27.
[50] K. Nakanishi, J. Porous Mater. 4 (1997) 67–112.
[51] Lawrence E. Kinsler, Austin R. Frey, Alan B. Coppens, James V. Sanders, Fundamentals of Acoustics, 4th ed., Wiley-VCH, 1999, p. 560.
[52] B.A. Auld, Acoustic Fields and Waves in Solids, Рипол Классик, Krieger Publ., Malabar, FL, 1973.
[53] L.L. Beranek, J. Acoust. Soc. Am. 13 (1942) 248–260.

[54] P.W. Bridgman, Dimensional Analysis, Yale University Press, New Haven, CT, 1922.
[55] F.B. Surani, X. Kong, D.B. Panchal, Y. Qiao, Appl. Phys. Lett. 87 (2005) 163111.
[56] B. Song, W. Chen, Exp. Mech. 46 (2006) 407–410.
[57] K.A. Dannemann, J. Lankford, Mater. Sci. Eng.: A 293 (2000) 157–164.
[58] P. Tan, S. Reid, J. Harrigan, Z. Zou, S. Li, J. Mech. Phys. Solids 53 (2005) 2174–2205.
[59] Y. Diao, T. Harada, A.S. Myerson, T. Alan Hatton, B.L. Trout, Nat. Mater. 10 (2011) 867–871.
[60] T. Kawaguchi, J. Iura, N. Taneda, H. Hishikura, Y. Kokubu, J. Non-Cryst. Solids 82 (1986) 50–56.
[61] C.J. Brinker, G.W. Scherer, Sol-Gel Science: The Physics and Chemistry of Sol-Gel Processing, Gulf Professional Publishing, Houston, TX, 1990.
[62] E.W. Washburn, Phys. Rev. 17 (1921) 273–283.